Integrated optical dual-cantilever arrays in silica on silicon

Peter A. Cooper*, Lewis G. Carpenter, Paolo L. Mennea, Christopher Holmes, James C. Gates and Peter G.R. Smith

Optoelectronics Research Centre, University of Southampton, Highfield Campus, SO171BJ, UK

*pac1g11@soton.ac.uk

Abstract: A dual cantilever device has been demonstrated which can operate as a force sensor or variable attenuator. The device is fabricated using physical micromachining techniques that do not require cleanroom class facilities. The response of the device to mechanical actuation is measured, and shown to be well described by conventional fiber optic angular misalignment theory. The device has the potential to be utilized within integrated optical components for sensors or attenuators. An array of devices was fabricated with potential for parallel operation.

OCIS codes: (130.3120) Integrated optics devices; (220.1920) Diamond machining; (220.4000) Microstructure fabrication; (230.1480) Bragg reflectors; (120.4880) Optomechanics.

References and links

1. A. Boisen, S. Dohn, S. S. Keller, S. Schmid, and M. Tenje, "Cantilever-like micromechanical sensors," Rep. Prog. Phys. **74**, 036101 (2011).
2. E. Ollier, "Optical MEMS devices based on moving waveguides," IEEE J. Sel. Top. Quant **8.**, 155–162 (2002).
3. K. Park, J. Jang, D. Irimia, J. Sturgis, J. Lee, J. Robinson, M. Toner, and R. Bashir, ""Living cantilever arrays" for characterization of mass of single live cells in fluids.," Lab on Chip **8**, 1034–41 (2008).
4. T. Xu, M. Bachman, F-G. Zeng, and G-P. Li, "Polymeric micro-cantilever array for auditory front-end processing," Sens. Actuators. A Phys. **114**, 176–182 (2004).
5. K. Zinoviev, C. Dominguez, J. A. Plaza, V. J. C. Busto, and L. M. Lechuga, "A novel optical waveguide microcantilever sensor for the detection of nanomechanical forces," J. Lightwave Technol. **24**, 2132–2138 (2006).
6. L. G. Carpenter, C. Holmes, H. L. Rogers, P. G. R. Smith, and J. C. Gates, "Integrated optic glass microcantilevers with Bragg grating interrogation.," Opt. Express **18**, 23296–301 (2010).
7. B. Barber, C. R. Giles, V. Askyuk, R. Ruel, L. Stulz, and D. Bishop, "A fiber connectorized MEMS variable optical attenuator," IEEE Photon. Technol. L. **10**, 1262–1264 (1998).
8. J. E. Ford, J. A. Walker, D. S. Greywall, and K. W. Goossen, "Micromechanical fiber-optic attenuator with 3 μs response," J. Lightwave Technol. **16**, 1663–1670 (1998).
9. A. Constable, J. Kim, J. Mervis, F. Zarinetchi, and M. Prentiss, "Demonstration of a fiber-optical light-force trap," Opt. Lett. **18**, 1867 (1993).
10. B. J. Black and S. K. Mohanty, "Fiber-optic spanner," Opt. Lett. **37**, 5030–5032 (2012).
11. M. Succo, "An Integrated Optical-Waveguide Chip for Measurement of Cold-Atom Clouds," Ph.D. Thesis, Imperial College London (2011).
12. T. Brown, "Harsh military environments and microelectromechanical (MEMS) devices," Proceedings of IEEE **2,** Sensors, 2003. 753–760 (2003).
13. N. Courjal, B. Guichardaz, G. Ulliac, J-Y. Rauch, B. Sadani, H-H. Lu, and M-P. Bernal, "High aspect ratio lithium niobate ridge waveguides fabricated by optical grade dicing," J. Phys. D (Appl Phys) **44**, 305101 (2011).
14. Y. Jia, C. E. Rueter, S. Akhmadaliev, S. Zhou, F. Chen, and D. Kip, "Ridge waveguide lasers in Nd:YAG crystals produced by combining swift heavy ion irradiation and precise diamond blade dicing," Opt. Mater. Express **3**, 433–438 (2013).

15. L. G. Carpenter, H. L. Rogers, P. A. Cooper, C. Holmes, J. C. Gates, and P. G. R. Smith, "Low optical-loss facet preparation for silica-on-silicon photonics using the ductile dicing regime," J. Phys. D (Appl Phys) **46**, 475103 (2013).
16. G. D. Emmerson, S. P. Watts, C. B. E. Gawith, V. Albanis, M. Ibsen, R. B. Williams, and P. G. R. Smith, "Fabrication of directly UV-written channel waveguides with simultaneously defined integral Bragg gratings," Electron. Lett. **38**, 1531–1532 (2002).
17. R. M. Parker, "Optofluidic Bragg Grating Sensors For Chemical Detection," Ph.D. Thesis, University of Southampton (2010).
18. R. M. Parker, J. C. Gates, M. C. Grossel, and P. G. R. Smith, "A temperature-insensitive Bragg grating sensor-Using orthogonal polarisation modes for in situ temperature compensation," Sensor Actuat. B Chem. **145**, 428–432 (2010).
19. C. Holmes, L. G. Carpenter, H. L. Rogers, J. C. Gates, and P. G. R. Smith, "Quantifying the optical sensitivity of planar Bragg gratings in glass micro-cantilevers to physical deflection," J. Micromech. Microeng. **21**, 035014 (2011).
20. B. G. Aitken and R. E. Youngman, "Borophosphosilicate glasses: properties and structure," Phys. Chem. Glasses **47**, 381–387 (2006).
21. H. L. Rogers, S. Ambran, C. Holmes, P. G. R. Smith, and J. C. Gates, "In situ loss measurement of direct UV-written waveguides using integrated Bragg gratings," Opt. Lett. **35**, 2849–2851 (2010).
22. A. Ghatak and K. Thyagarajan, *An Introduction to Fiber Optics* (CUP, 1998), p. 154.

1. Introduction

The use of Micro-Opto-Electro-Mechanical Systems (MOEMs) in integrated optics promises devices with improved performance, compactness and greater functionality. The cantilever is a common element within microstructures with mechanical properties that make it especially well-suited to function as a sensor or actuator [1]. MOEM devices using a single cantilever have been demonstrated previously, for example, where a moveable waveguide is displaced relative to a fixed waveguide. Ollier *et al.* fabricated an optical switch based on silica-on-silicon technology that used electrostatic switching to function as a switch between channel waveguides [2]. While single cantilevers provide a way to create devices, the use of dual cantilevers has been pioneered by Park *et al.* as a way of attracting cells to adhere to a cantilever, whereon they can be cultured and weighed using a resonance frequency method [3]. In another example of this geometry Xu *et al.* fabricated dual cantilevers in polymer, which also served as waveguides, in a device that functioned as an acoustic sensor [4].

Various schemes are well known for transducing mechanical motion onto an optical signal. For example, a small mirror mounted on the cantilever will deflect a laser beam, an approach widely deployed together with quadrant detectors in atomic force microscopy. However, all free space optics are susceptible to their local environment, for example temperature, airflow, vibration, shock, *etc.*, and a well-known advantage of integrated optics, beyond the simple factor of compactness, is robustness and reduced cross-sensitivity. Thus, if the components for optical sensing can be integrated into the cantilever then this can have benefits for the performance and compactness of the device. The integration of optical components into a glass cantilever for force sensing has already been demonstrated by Zinoviev *et al* [5]. Carpenter *et al.* [6] incorporated two Bragg reflectors into a glass cantilever to create a cavity. In that work deflection of the cantilever caused a change in the optical path length of the cavity thereby modifying the optical spectrum which was used to determine the deformation.

Beyond sensing, fiber based variable optical attenuators have been demonstrated by Barber *et al* [7]. They used a voltage-controlled moving mirror MEMS device to achieve up to 50dB of attenuation. Ford *et al* fabricated a MEMS device which used a silicon nitride quarter wave plate to realize a variable reflective mirror [8]. Their device exhibited 25 dB of dynamic range with an insertion loss of 3 dB. Another area where the dual-cantilever geometry is employed is in the domain of particle trapping. Constable *et al.* first demonstrated an optical light trap configuration comprising of only two optical fibers

avoiding the use of any other optical elements [9]. They indicated that angular displacement of the fibers allows the trap position to be moved. Black *et al.* [10] further showed that translational displacement could be used to give controlled rotation of smooth muscle cells. As well as applications in biological science, Succo *et al.* demonstrated a monolithic implantation of a cold atom trap [11] using dual waveguides. A dual-cantilever version of this device could be used to provide better physical access for probing of the atom, and offers potential for microscopic adjustment of trap parameters. In this report, we describe a dual-cantilever device, fabricated and characterized for the first time in silica-on-silicon. The new devices in this work are larger in cross-section than conventional MEMS leading to greater bending stiffness and high resonant frequencies. While high stiffness requires greater force to actuate, it can be advantageous in providing better immunity to acoustic noise or vibration and thus can be desirable for attenuator, switching or trapping applications. Furthermore, in some MEMs applications in harsh environments, e.g. projectiles, accelerations of up 100,000g occur and more robust MEMs structures may have advantages [12]. The lack of free space optics combined with the potential for multiplexed sensing could make possible the use of this type of device in field applications.

Currently photolithographic techniques dominate in the fabrication of MOEM devices. While this fabrication approach has many benefits including parallel processing and small feature size, it requires access to cleanroom facilities, and such access to appropriate equipment can be expensive and be energy intensive. An alternative to lithography for fabrication is based on physical machining, and is developing rapidly as tools and systems become available. Mechanical dicing has been demonstrated in a range of materials and formats such as lithium niobate [13] and Nd:YAG [14]. In the dual-cantilever work in this study, we used the physical dicing technique which can give optical-quality surface-roughness with low processing times. The surface quality of the machining technique has been previously demonstrated in silica-on-silicon photonics using the ductile dicing regime [15].

2. Design and experimental realization

Fig. 1. Shows a 3D visualization showing the concept of dual opposing cantilevers machined into silica-on-silicon. Each cantilever contains an optical waveguide. The cantilevers are produced using dicing technology and etching away silicon to release the silica structures.

The dual cantilever arrangement shown in Fig. 1 consists of a neighboring pair of cantilevers with each cantilever containing a waveguide. The devices are fabricated in silica-on-silicon and the details of the fabrication will be described in detail later. When both cantilevers are deflected, this changes the relative angle between them and hence the coupling of light between the launching waveguide and the receiving waveguide. This section will describe the fabrication steps, as well as design considerations that affect the performance of the device. The underlying substrate is a silicon wafer of <100> orientation of 1mm thickness, providing a robust starting platform. The key techniques in the fabrication of the cantilevers are a micromachining process using a dicing approach and wet etch with potassium hydroxide. The optical glass is deposited onto the silicon substrate via Flame Hydrolysis Deposition (FHD). A thermally grown layer of oxide on the silicon wafer acts as an underclad layer and has a thickness of 15 µm. On top of this layer a core layer of silica glass is deposited using FHD and is doped with germanium and boron to promote photosensitivity. A cladding layer is then deposited which is doped with phosphorous and boron to provide a lower consolidation temperature relative to the core. After each layer is deposited it is consolidated in a furnace at temperatures between ~1200° C and ~1360° C. The channel waveguide will be later formed in the core planar layer. Although high temperatures are required during the fabrication of the substrate, other devices, such as MEMS, could be integrated upon the substrate but only post consolidation. The high processing temperatures result in a very physically and chemically robust platform.

To create the cantilevers a Loadpoint Microace dicing saw was used to define 7 grooves through the silica and into the silicon. A nickel-bonded blade with a width of 100 µm impregnated with 4000 grit diamond abrasive was used (ZH05-SD4000-N1-50 KK). A plunge-cut mode was used which consists of the blade coming vertically downwards onto the workpiece without any translation. Fig. 2(a) shows the structure after the dicing steps. As plunge-cutting is more susceptible to blade breakage and top-edge chipping, optimization was required to avoid these issues. A plunge speed of 5 µm/s and spindle speed of 20 krpm were found to reduce chipping to an acceptable level. Due to the circular blade shape, the resultant grooves are crescent shaped with the silicon only being exposed at the center where the grooves are deepest. As seen in the image the exposed silicon at the center shows higher reflectivity than the exposed silica due to lower surface roughness and increased Fresnel reflection. This is illustrated by the graphic in Fig. 2a.

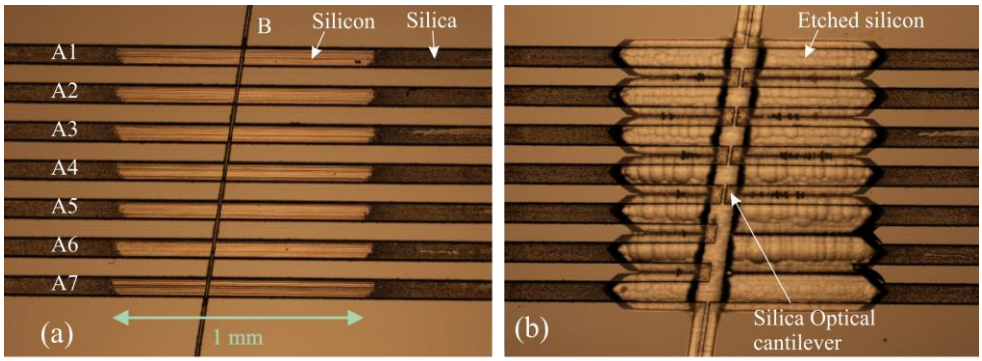

Fig. 2a. The image shows an optical microscope (top-side) image of the glass cantilevers before etching. 7 parallel grooves are diced using a plunge method technique (labelled as A1-A7 on the image). The silicon substrate is observed in the middle of the grooves and highlights the crescent shape. A second channel (B) is diced at an angle of 8° from perpendicular to the previous grooves which was in a conventional non-plunge mode. Fig 2b shows the glass cantilevers after etching. The regions of exposed silicon are removed by the KOH etchant, resulting in the lighter coloured central regions. The overlaying optical cantilevers are essentially transparent but can be seen most clearly in the region of the central channel.

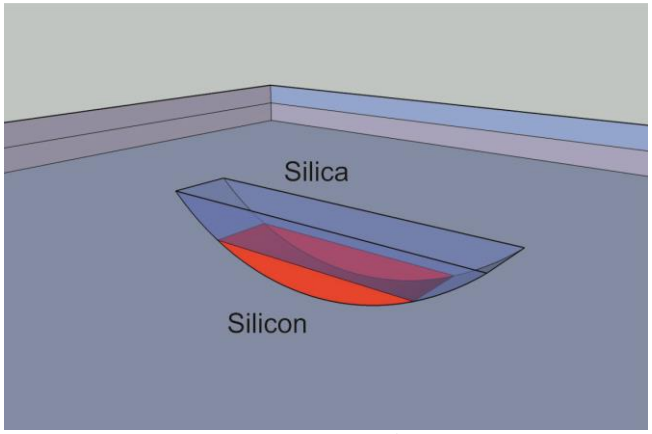

Fig. 3. Image shows a 3D visualization of the crescent shaped plunge-cut illustrating that the silicon becomes exposed only in the central region of each cut. This is important as the silicon etches much faster with KOH, so it is this exposed region that undercuts the overlying adjacent silica to create the cantilevers.

To create the dual cantilevers a second groove (B) is diced with a 15 µm width blade at an angle of 8 degrees from perpendicular to the previous grooves. Having the end facets of the cantilevers at this angle ensures that the reflected light exceeds the numerical aperture of the guide, which could lead to fringes in the measured spectrum. The previously reported direct UV writing process [16] is used to simultaneously define the waveguides and Bragg gratings. 9 Bragg gratings are written along the waveguide with various periods which will be used for characterization. The waveguides were written after the dicing but before the wet-etch described in the next section. Using the UV fluorescence from the sample, the waveguides and Bragg gratings were precisely aligned to the diced grooves. The thickness of the core FHD layer was measured using a Metricon prism coupling system to be 5.4 µm. This defines the vertical dimension of the waveguide core. The horizontal dimension is controlled by the UV writing spot size and the applied fluence. These parameters have been adjusted to match the mode size to standard single mode optical fiber and hence the mode field diameter at 1550nm is ~10um in the vertical and horizontal directions. The resulting waveguide is single mode which is confirmed by the single Bragg peaks observed during spectral characterization. This data also confirms that the waveguides have little birefringence and indicates that the two polarization modes have similar modal dimensions. This is also confirmed by modelling with a commercial modelling program Fimmwave (Photon Design Ltd). More details of this modelling and optical mode measurements can be found elsewhere [17,18]. The dimensions of the cantilevers were designed such that the core mode was more than 17 µm away from any lateral surfaces to ensure that the mode was not affected by the external environment. Finally, the chip was wet-etched in 25% potassium hydroxide solution at 75^{o}C for 5 hours to preferentially remove the silicon and release the glass cantilevers from the substrate. A comparison of the device pre and post etching can be seen in Fig. 2.

The cross-sectional area of the cantilever is 100µm × 40µm. The channel waveguide runs through the cantilever such that it is centered about the vertical and horizontal neutral axis. This minimizes strain induced refractive index and physical length variations upon actuation. [19].

Fig. 4 shows a Scanning Electron Microscope (SEM) image of the released cantilevers after etching. At the stage of wafer fabrication the glass layers are all under compressive stress due to the lower coefficient of thermal expansion of the glass compared to the

silicon. In addition, stress in each layer of the glass differs due to the different doping levels and also their consolidation temperatures. For example the thermal expansion coefficients vary between ~5.5×10^{-7} K^{-1} for pure silica, representative of thermal oxide, and up to 4.3×10^{-6} K^{-1} for borophosphosilicate [20]. This differential is evident in Fig. 4 where upon release the micro-cantilevers deflect out of plane. Thus cantilever curvature can be controlled through a combination of layer thicknesses, cross-sectional form, or directly manipulating stress in the layers through changing dopant concentrations and consolidation temperature of the FHD process.

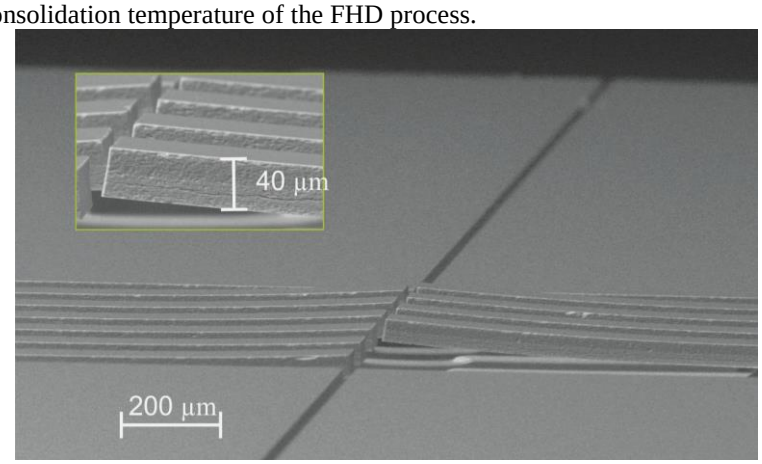

Fig. 4. SEM image of the etched cantilever device. Note that first two cantilevers at the right side of the image sustained damage during the etching / drying process, however, this enables a clear visualization of the side walls of the third cantilever (shown in the inset image). The deflection out of the plane occurs because of stress inherent in the layers due to their high consolidation temperature.

The inset of Fig. 4 shows a side wall image of one of the cantilevers. The device was further characterized with a Zemetrics Zescope optical profiler and results are shown in Fig. 5. These measurements show that the form of the intrinsic displacement was essentially the same for each cantilever. For the set of cantilevers the resultant intrinsic displacement after fabrication ranged from 5μm to 17μm for the shortest and longest devices respectively. Due to the 8º crosscut used to form the dual cantilevers, the cantilever pairs have varying levels of length mismatch. The main cause of variation in the form, is due to the position of the root which is affected by the KOH etching conditions. The limiting factors for the size of cantilever that could be produced by this method are the lateral positional accuracy of the dicing saw used and the physical strength of the machined ridge. Were the width of the cantilever to become too narrow the interaction between the optical mode and the sides of the cantilever would increase, risking additional loss.

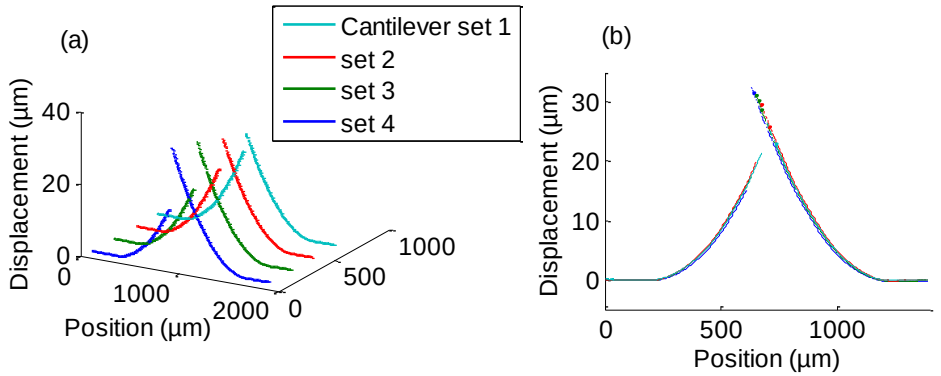

Fig. 5. Profiles of cantilevers showing out-of-plane displacement without load (due to the release of intrinsic stress) Fig. 5a shows deflection of each cantilever measured with the Zescope optical profiler. The length mismatch results in differing maximum displacements. Fig. 5b shows the same data but with the curves overlapped, effectively an isometric view of Fig. 5a. The shapes are very consistent with only a difference in final height between the curves.

A finite element simulation (FEM) model was run using COMSOL Multiphysics software. A three stage model was built that first simulates the thermal oxide and FHD glass depositions to simulate the thermal stresses that are built up once the consolidated glass layers are cooled to room temperature. The 3rd stage was to model the out of plane deflections once the cantilevers are freed from the silicon substrate. The following values were used for the thermal expansion coefficients. Silicon: 2.5×10^{-6}. Thermal oxide silica: 0.55×10^{-6} K^{-1}. Cladding layer glass (borophosphosilicate): 4.3×10^{-6} K^{-1}. The results from the COMSOL simulation are shown in Fig. 6.

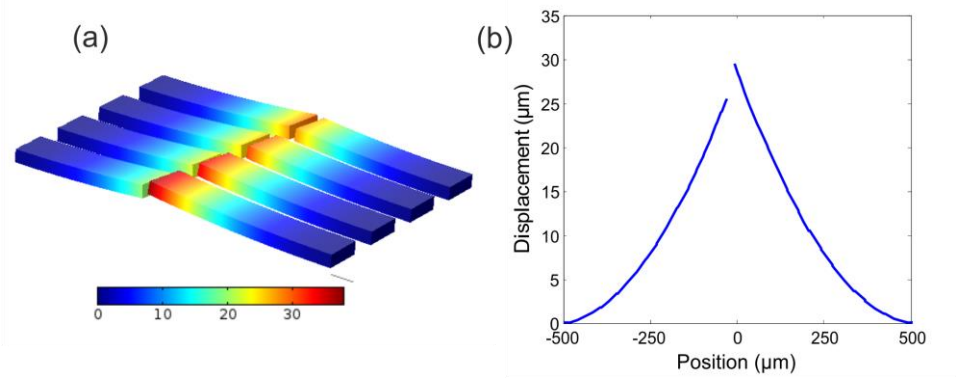

Fig. 6a. Comsol simulation showing out-of-plane displacement following etch release (in microns). 6b The displacement cross-section through the pair of cantilevers most equal in length. The parameters of the simulation are listed in the text.

To compare the model with the experimental data the out-of-plane deflection of cantilevers forming set 1 was studied. The model predicted 25 and 29 µm for the two cantilevers, while for the real device the deflections were 19 and 26 µm. It is believed that this difference is because the true coefficient of thermal expansion of the cladding layer is not known with high accuracy. However the reasonable accuracy of the model suggests that the biggest contribution to the bending is the higher thermal coefficient of expansion of the FHD cladding glass compared to the thermal oxide.

3. Results and discussion

Having fabricated the dual cantilever containing waveguides and Bragg gratings, the loss was measured using an approximation of the grating based method [21]. The location and wavelengths of the Bragg gratings are shown in Fig. 7.

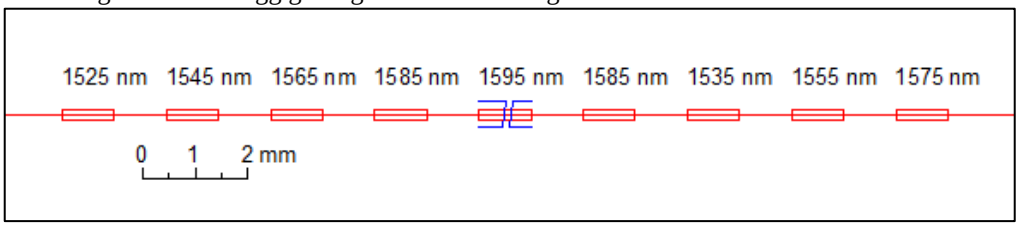

Fig. 7. A schematic showing the locations of the waveguide and Bragg gratings in relation to the cantilevers. Red: Bragg gratings and waveguide. Blue: Cantilevers. The gratings are 1mm in length and separated by 1mm. The total cantilever section length is also approximately 1mm and only affects the 1595 nm grating. The total device size is 10mm × 20mm.

The optical spectrum of the device was measured in reflection using a broadband source and Optical Spectrum Analyzer (OSA) as shown in Fig. 8.

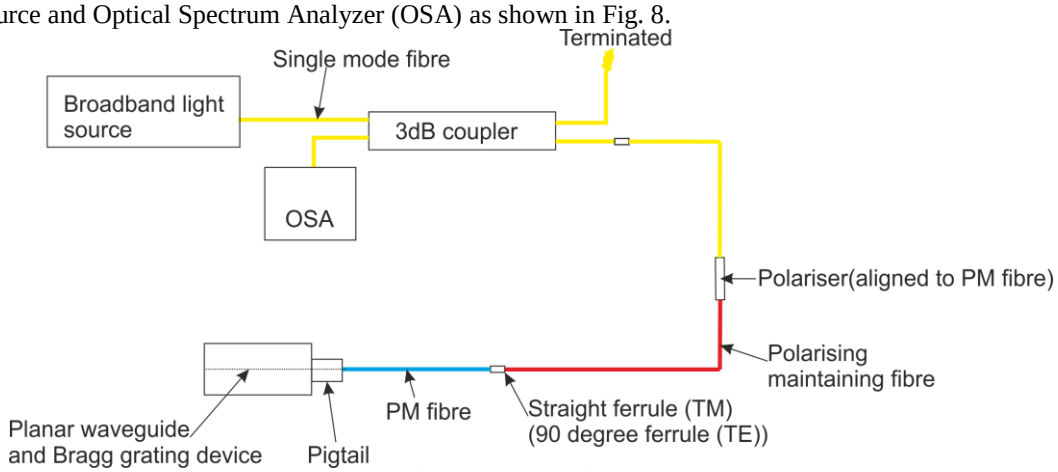

Fig. 8. Optical setup used to characterize the reflection properties of the devices. A polariser aligned to a PM fiber ensures spectrally independent polarised source.

Polarization maintaining optical fiber components and a polarizer are used so that the two orthogonal polarization modes can be measured separately. Fig. 9 shows the spectra for the TE and TM modes. The reflectivity is normalized to the source power and includes the coupling loss due to the fiber-optic pigtailing. There is a loss between the cantilevers due to the Fresnel reflections at the two interfaces (calculated to be ~0.3dB). There is also loss from the lateral misalignment caused by the 8º interface and is calculated to be ~0.6 dB. The two gratings at 1585nm form a Fabry-Pérot cavity. The fringes from this are clearly visible in Fig. 9 but will not be used in this work. The effective indexes of the TE and TM modes at 1550 nm are 1.44823 and 1.44847 respectively. This birefringence is due to in-plane thin film stress caused by the mismatch in thermal expansion coefficients between the silica and silicon. This corresponds to birefringence of 2.36×10^{-4}. This effect is due to the stress-optic effect creating anisotropic refractive index, with the TM mode exhibiting a higher refractive index.

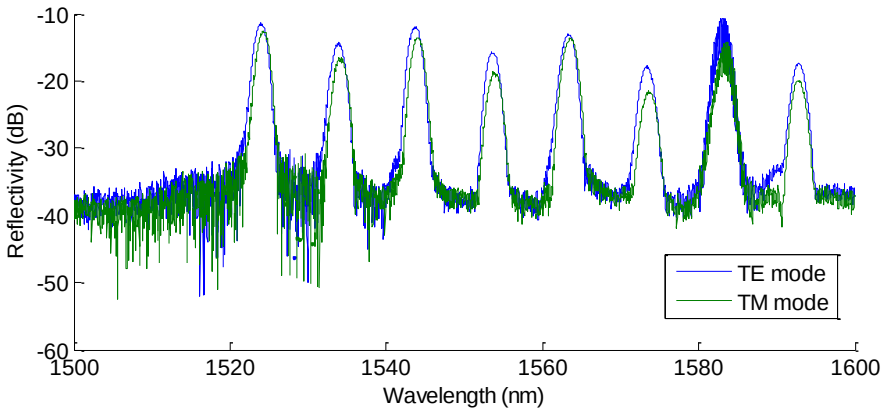

Fig. 9. Reflection spectra taken after dicing but before etching. The data shows the absolute reflectivity calibrated against a known fiber end reflection. Analysis of the peaks shows a wavelength shift due to birefringence of 0.28 nm.

After etching the cantilevers are released, without load the misalignment becomes large and effectively zero signal is seen from the gratings beyond the diced groove. This is to be expected as the dual cantilevers were all asymmetric in length and so without load sit at different heights. The robustness of the cantilevers allows them to be deflected using an external load thereby bringing the waveguides into alignment. In the next section measurements will be presented demonstrating this operation.

To test the optical response of the cantilevers to actuation, an optical fiber was used to deflect the cantilevers as it could be easily cleaved to give a perpendicular end facet, as well as benefitting from having a small diameter which restricts the contact area to be close to the ends of the cantilevers. The device was mounted on a flexure translation stage (Thorlabs 3-Axis NanoMax Stage) which allowed X, Y and Z positioning with sub-micron precision. Two modes of actuation are possible: to push both cantilevers simultaneously or to only deflect one as shown in Fig. 10(a) & (b) respectively. In this paper a positive displacement corresponds to the cantilevers being pushed into the plane of the device. Fig. 11 shows camera images of the device taken during the experiment.

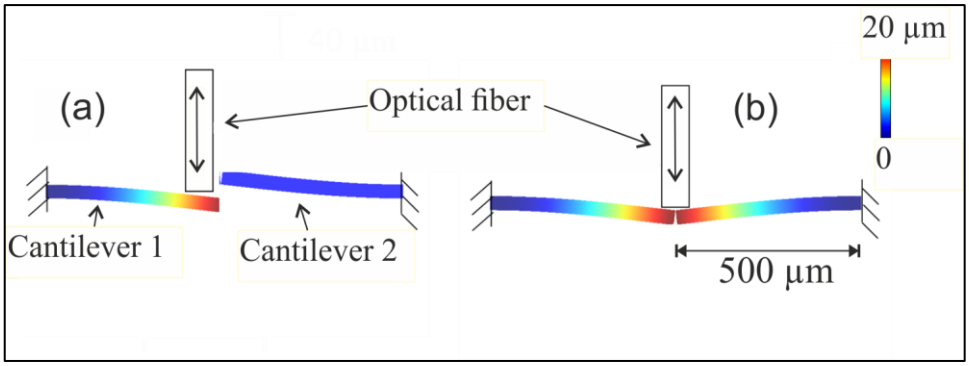

Fig. 10. Showing the two possible types of actuation. The colour maps calculated in Comsol indicate the displacement of the cantilever from its rest state. The colour bar shows the displacement in microns.

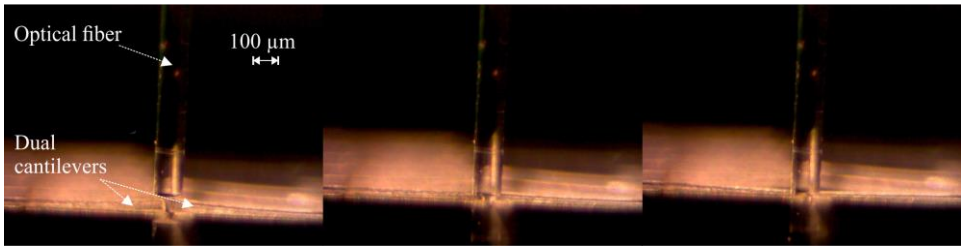

Fig. 11. Camera images showing physical actuation of the cantilevers with an optical fiber pushing down on the cantilever with different heights of actuation. An optical fiber was used as it is only 125 micron and provides a stiff small cross-section rod.

Fig. 12 shows a comparison of the TE spectra for the actuated and rest states. Upon actuation the two cantilevers can be aligned, such that light couples between them. This is observed in as upon actuation the Bragg reflections from both cantilevers can be seen. Those marked with the label 'A' are on the side of the device coupled to the optical fiber while those labeled 'B' are on the other side. The peak labeled 'C' is from the Fabry-Perot cavity whilst the grating giving peak 'D' is located in the cantilevers. There is also an increase of approximately 10 dB in the background level due to increased broadband Fresnel reflection from the facet of the second cantilever.

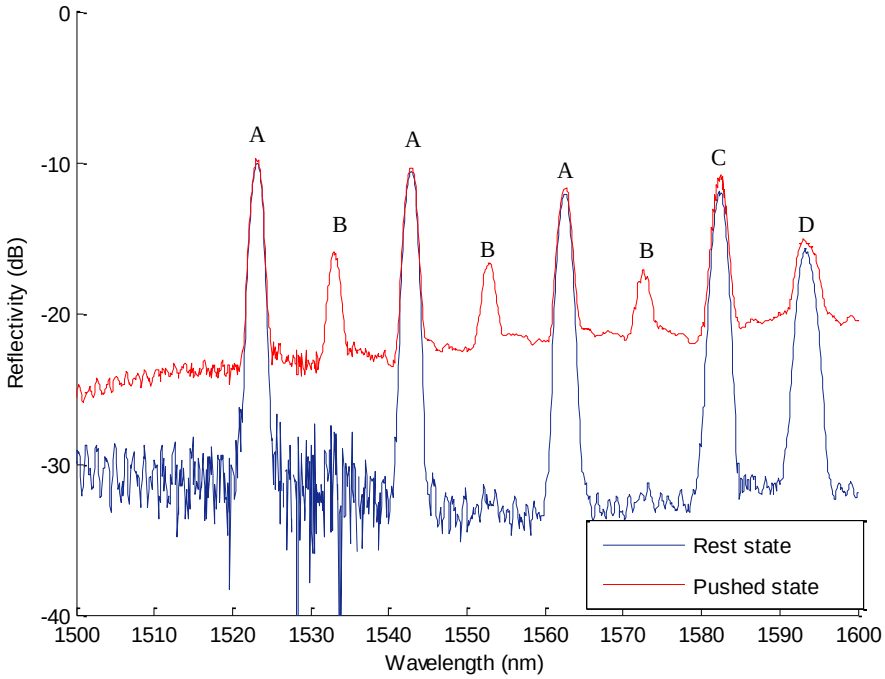

Fig. 12. The measured TE spectra of the device in the rest state (blue), and a deflected state (red). Actuating the devices increases the reflectivity of Bragg gratings opposite to the coupling side. As can be seen it also increases the background level by approximately 10dB. The Bragg gratings labelled with 'A' are on the side of the device coupled to the optical fiber while those labelled 'B' are on the other side.

The optical coupling between the cantilevers is determined by the angle between them. By measuring the transmitted intensity it is possible to measure the coupling. However by using the reflectivities of the Bragg gratings it is also possible to measure them in a way

which is insensitive to fluctuations in source power and requires only coupling to one waveguide facet. Peak intensities are fitted to Gaussian apodized Bragg gratings (1555nm and 1565nm) on each side of the central cavity and used to give a relative reflectivity which is only dependent on the optical coupling between the cantilevers. The insertion loss at the maximum coupling point can be obtained by measuring the spectrum from both ends of the device. [21]. The measured minimum coupling losses were 2.4±0.1 dB for the TM mode and 2.8±0.2 dB for the TE mode. The data suggests that there may be a greater loss for the TE mode, but as the difference is only 1.7σ this may not be statistically significant. The slightly greater numerical aperture of the TM mode, due to birefringence, may contribute to this difference.

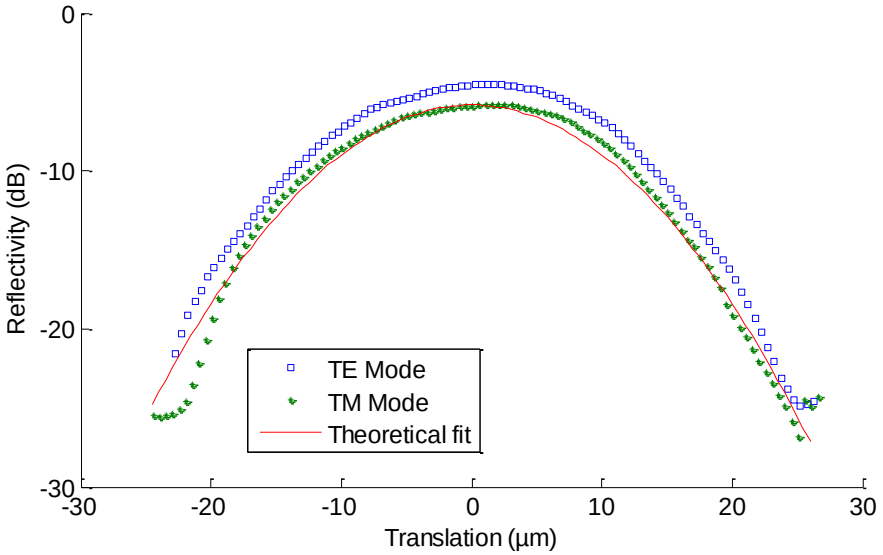

Fig. 13. Plot showing the ratio of reflectivity from Bragg gratings on opposing sides of the dual cantilevers (relative reflectivity) versus the displacement of both cantilevers. The theoretical fit makes use of equation (1).

Fig. 13 shows the coupling as both cantilevers are pushed simultaneously. The zero value for translation is obtained by fitting the quadratic misalignment loss curve after the experiment. It can be seen that the optical coupling goes through a maximum which occurs for a certain angle between the cantilevers. This is expected to be 0º, however error in the angle of the facets from the fabrication processes may give an offset. The geometry is related to the problem of loss due to angular misalignment between two fibers [22]. Here the misalignment angle is taken to be twice the angle of rotation of a single cantilever. The loss in dB is given by eq (1).

$$\alpha_a\left(dB\right) = 4.34\left(\frac{\pi n_l w\theta}{\lambda_0}\right)^2 \tag{1}$$

Here α_a is the loss in decibels, n_l is the refractive index of the medium between the fiber ends, θ is the angle of misalignment, λ_0 is free space wavelength and w is the spot size of the mode. This loss figure (given in dB) is derived from the overlap integral of the mode exiting a first fiber being coupled into the input mode of a second fiber. The mode size w of the UV written waveguide, is approximated as 5 µm which is similar to SMF28 single mode optical fiber.

Actuating a single cantilever was also accomplished, and similarly, shows a coupling peak as seen in Fig. 14. The peak is asymmetric once the actuated cantilever moves below the second cantilever, which suggests coupling from cladding modes back into the core

mode. This is thought to be as a result of the curvature of the cantilevers and the angled interface of the receiving cantilever which remains deflected due to the intrinsic stress. Once the deflected cantilever is below the receiving cantilever coupling is still possible due to refraction and scattering resulting in an asymmetric peak. The sensitivity of relative reflectivity to translation over the central 10 µm of the fitted model is 0.16 dB/µm.

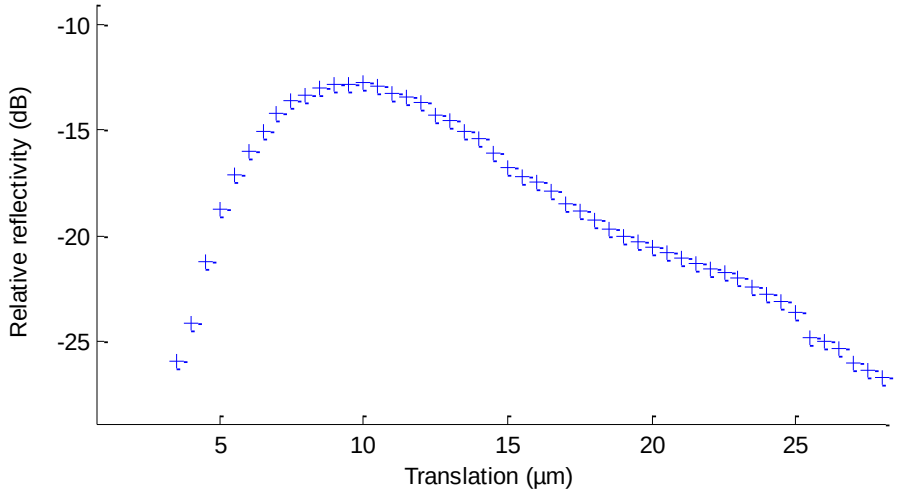

Fig. 14. The relative reflectivity response of a single cantilever translation also showing a point of maximum coupling for the TE mode. It is however less symmetric which suggests that there is coupling to the fundamental mode through cladding modes and due to the lack of verticality of the receiving cantilever end facet. Scatter may also contribute to this asymmetry.

The experiment was also carried out using the transmitted intensity. For this experiment the device was pigtailed with optical fibers at both ends of the waveguide using UV curing glue. The spectra are shown in Fig. 15 and again show good agreement to the theoretical coupling efficiency. This experiment was then repeated with the device covered with refractive index oil of n = 1.46. This modifies the gap refractive index and shows the expected change of making the peak narrower with a higher transmission (1.13 dB) as the Fresnel reflection is reduced. Furthermore, diffraction is reduced in the higher index oil leading to a narrower width. In addition the higher refractive index of the oil will tend to strip cladding modes reducing excitations at larger displacement. The deviation of the experimental data from the model is observed at larger displacements corresponding to lower light levels at 15 dB below the peak transmitted signal due to both background scatter and excitation of cladding modes. This effect was not observed in the reflection data of Fig. 13 due to the high return loss of the device.

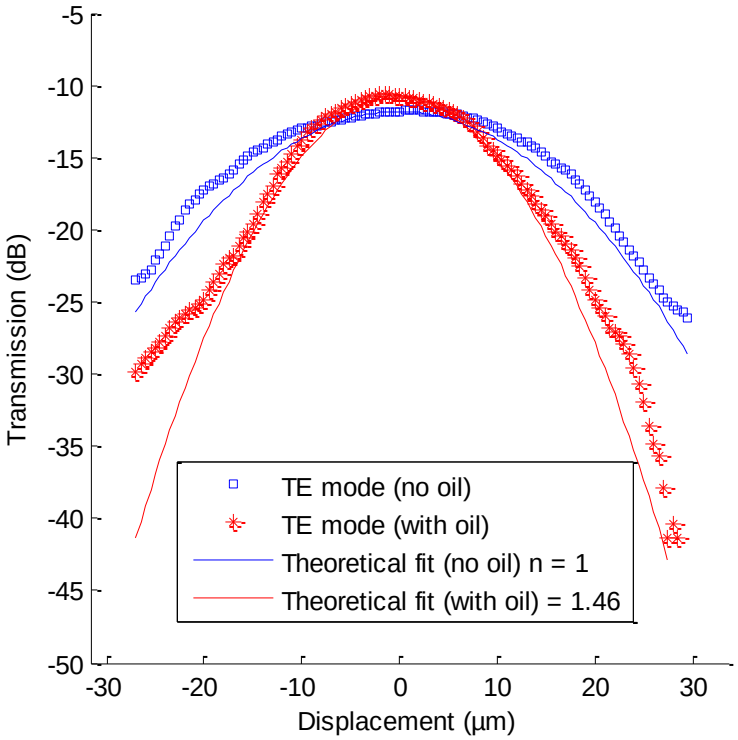

Fig. 15. Transmission during double push actuation showing effect of immersion in oil n = 1.46. The total transmission is improved with oil as would be expected from reducing off scatter and Fresnel loss. The peak narrows because the output beam does not diffract as rapidly so the receiving fiber position becomes more critical.

4. Conclusion

A new approach of fabricating dual cantilever devices has been demonstrated, utilizing precision dicing technology, direct UV writing and selective wet etching. The approach makes use of physical micromachining techniques that do not require cleanroom class lithographic and etch facilities. The devices are shown to operate in a mode suitable for a displacement sensor or with the addition of an actuator, such as a piezo-electric, a MOEMS variable attenuator. By investigating the response of the device to actuation with an optical fiber we have shown that the mechanical-optical behavior of the device is well described by conventional fiber optic angular misalignment coupling theory.

The device contained an array of four dual-cantilevers, demonstrating potential for creating parallel arrays for switching or sensing applications. The signals from these arrays could be wavelength multiplexed with the use of Bragg gratings. Each cantilever contained nine discrete Bragg gratings, so the overall device incorporates many integrated elements on a single chip. These devices offer potential for use in switching, optical attenuators, and optical trapping. Their greater stiffness makes them attractive for use in harsh environments, and they may be embedded in composite materials where the higher required actuation forces are readily achievable. Furthermore, as they are waveguide devices they avoid the alignment issues inherent in free space measured structures.

Acknowledgments

We would like to acknowledge the support of the Engineering and Physical Sciences Research Council (EPSRC) for supporting this work.